Check for updates

Photodegradation-driven microparticle release from commercial plastic water bottles

Hannah Folarin, [ID] Nyiri Hajian, [ID] Kirby Hill and Alexander Laskin [ID] *

Plastic pollution is widespread in the environment and has been detected in natural and drinking water sources. In this study, seventy polyethylene terephthalate (PET) bottles with five different wall thicknesses were exposed to sunlight for ten weeks to evaluate the role of photochemical degradation as a potential source of microplastics in bottled drinking water. Solar flux measurements were used to calculate the cumulative photon dose received by the bottles, which enabled the extraction of apparent first-order reaction rates for microparticle formation as detected by flow immersion microscopy. Buildup of microparticles was observed up to $14–20~\mu g~L^{-1}$ during the first 30 days of the experiment, corresponding to a cumulative UVA + UVB photon dose of $\sim 30 \times 10^{24}$ photons cm^{-2}, followed by a plateau at higher photon doses. The observed plateau is likely due to a combination of factors, including the limited extent of the water–plastic interface susceptible to decomposition induced by photolysis and continued photodegradation and breakdown of previously released microparticles into smaller, sub-detectable fragments. Fourier-transform infrared spectroscopy analysis of plastic bottles before and after sunlight exposure revealed carbonyl $_\nu[C{=}O]$ stretching band reductions, indicating chemical degradation through bond scission and decarboxylation. Comparative analysis of the spectroscopic and kinetic data suggests that PET with higher amorphous content is more susceptible to photochemical degradation, leading to accelerated breakdown and increased microplastic release. High-resolution mass spectrometry analysis of filtered microparticle samples revealed repeating units of terephthalic acid and ethylene glycol (*m/z* 192.035), consistent with the primary monomer unit of PET polymer. Furthermore, the mass spectra of the filtered microparticle material closely resembled that of PET, sharing many of the most abundant spectral features. These findings confirm that the microparticle residues detected in the bottled water originated from the plastic material.

1. Introduction

Microplastic particles are widespread and persistent environmental pollutants in terrestrial and aquatic systems.[1] These tiny plastic particles originate from various sources, such as consumer products, industrial processes, and the decomposition of larger plastic waste.[2–4] In recent years, research on microplastic pollution has grown significantly, with studies focused on the sources, distribution, and ecological impacts of these particles on various environments.[5,6] Microplastics originate from a variety of sources,[1] but a major contributor is the biogeochemical degradation of large plastic items, such as commercial plastic containers and water bottles, which are ubiquitous in daily life.[7,8] Plastic water bottles, widely used as single-use items, can degrade over time under environmental conditions, such as sunlight exposure, resulting in photodegradation.[7,9–11] This degradation not only compromises the structural integrity of the

plastic but also facilitates the release of hazardous chemicals, transforming otherwise innocuous plastic bottles into potential sources of microplastic and contributing to the growing burden of environmental microplastic pollution.[10–12]

Recent studies have highlighted potential concerns related to microplastics in drinking water and their implications for human health and environmental safety. For example, a typical liter of bottled water has been reported to contain an average of 240 000 detectable plastic fragments smaller than 1 μm, which is 10 to 100 times higher than earlier estimates based solely on larger super-micrometer-sized particles.[13] Other studies have identified microplastics in tap and reservoir water, with their sources being larger plastic items degrading into smaller particles.[14,15] Exposure models suggest that drinking microwaved water could lead to microplastic ingestion at a level of 20.3 ng kg^{-1} daily.[16] These findings indicate that common drinking water sources can contribute to microplastic exposure.[17,18] Identifying and quantifying these sources is essential to understanding the broader impacts of microplastic contamination better.

Department of Chemistry, Purdue University, West Lafayette, IN, USA.
E-mail: alaskin@purdue.edu

Solar water disinfection (SODIS) is a common method of purifying water in regions with sufficient solar radiation and limited access to clean water.[19–21] This method involves filling clear plastic bottles, typically made of transparent poly(ethylene terephthalate) (PET), with contaminated water and exposing them to sunlight for several hours to inactivate pathogens such as bacteria, viruses, and protozoa.[20–23] However, the potential release of microplastics from SODIS containers due to photodegradation remains underexplored. Emerging studies suggest prolonged sun exposure can lead to microplastic release from PET and polypropylene (PP) containers.[20,24,25] While this effect may be minor in the short term, it raises important questions about the long-term sustainability and safety of SODIS. Therefore, systematic evaluation and quantification of microplastic formation during the sunlight exposure of bottled water are necessary to assess potential environmental impacts and risks from microplastics in sunlight-treated drinking bottled water. In particular, a critical knowledge gap remains regarding the extent to which sunlight-induced degradation of plastic bottles contributes to microplastic generation.

Microparticles have been extensively characterized using spectroscopic and microscopic methods, providing valuable insights into their morphology and composition.[26,27] Flow immersion microscopy offers automated particle detection and imaging, enabling accurate and high-throughput evaluation of microparticle formation.[28] In this technique, a sample is passed through a narrow cell where particles are individually illuminated and imaged as they traverse the optical field of view. This allows for detailed morphological analysis and rapid acquisition of microparticle size data with sufficient statistical depth to analyze large particle populations.[28–30]

In this study, we present an experimental investigation of the photodegradation of commercial PET water bottles under solar irradiation. Flow immersion microscopy was used to quantify the size distribution and mass concentration of released microparticles. Additionally, we examine the influence of UV intensity, exposure duration, crystallinity and bottle wall thickness on microparticle formation, providing a quantitative assessment of microparticle release from PET bottles commonly used for bottled drinking water.

2. Experimental methods

2.1. Sunlight exposure experiment

Five types of commercial drinking water PET plastic bottles, each with different wall thicknesses, were used in this study. (SI1, Fig. S1). Each bottle retained its original commercially bottled water, without replacement or refilling. The bottles varied by brand and wall thickness, reflecting consumer variability. No attempt was made to standardize additives or polymer grades, ensuring a realistic representation of the commonly used bottled water. Bottles from the same large pack batches were placed on the rooftop of the Brown Herbert C. Laboratory of Chemistry (approximately 15 m tall), Purdue University, West Lafayette, IN (40.4259° N, 86.9081° W) where they were exposed to natural sunlight for 70 days during the summer of 2023

(05/30/2023 – 08/08/2023) (SI1, Fig. S2). Four bottle types contained regular drinking water (pH 6–8), while the fifth contained lemon-flavored water (pH 3) (SI2, Fig. S3). Sets of five bottles were collected at regular intervals beginning on the third day of exposure and stored in the dark until analysis.

2.2. Solar flux measurement

Incoming sunlight radiation was measured using a StellarNet Miniature Fiber Optic Spectrometer (StellarNet Inc. USA). Wavelength-dependent spectral irradiance data (W m^{-2}) were recorded with SpectraWiz software and converted to photon flux (photons per cm^2 per s) using eqn S1 (SI3). This conversion enabled direct comparison with modeled solar actinic flux data. Hourly and daily photon fluxes observed in this study are shown in SI3 (Fig. S4a). Solar actinic fluxes for West Lafayette, IN, were modeled in the 280–400 nm range at 1 nm resolution using the TUV calculator, with default settings for overhead ozone column, surface albedo, ground elevation, and atmospheric conditions (clouds and aerosols). (**https://www.acom.ucar.edu/Models/TUV/Interactive_TUV/**). For comparison, solar actinic fluxes were also modeled for a representative SODIS region (Almeria, Spain, 37.0947 N, −2.3584 W), as shown in SI3 (Fig. S4b). Finally, photon fluxes were integrated over time and converted to cumulative photon dose (photons per cm^2) using eqn (S2) (SI3), reflecting the total number of photons received per unit area during the exposure period.

2.3. Flow immersion microscopy measurements

Each plastic bottle with water was shaken, and a 0.2 mL aliquot was analyzed using a FlowCam® Nano instrument (Yokogawa Fluid Imaging Technologies Inc.) operated with Visual Spreadsheet 6.0.3 software. The software automatically captured and processed particle images for visualization and analysis. Prior to each experiment, the instrument was autofocused with the NIST Traceable Polymer Microspheres (Catalog number: 3K-700), with a known mean diameter of 0.702 ± 0.006 μm and a density of 1.05 g cm^{-3}. Instrument settings were a 40× objective lens, a 1.4 numerical aperture condenser, and a flow cell with dimensions of 60 μm depth × 500 μm width. Additional imaging parameters were: 0.1 μm minimum distance to nearest neighbor, auto image capture rate of 137 frames per s, light/dark threshold of 20/20, a single iteration of hole-closing, and a particle size detection range of 0.3–60 μm. Background intensity levels in all experiments were recorded in the range of 172–175. Each analysis run typically detected an average of over ten thousand particles per fluid imaged.

Particle number concentrations were determined using the count calibration mode under the instrument settings listed above, with a flow rate of 0.02 mL min^{-1} and a sampling duration of 10 min. Measurements were performed in triplicate. Before each measurement, the flow cell was rinsed with 0.20 mL of filtered Windex® solution, followed by a rinse with deionized water to eliminate residual particles and prevent cross-sample contamination. Two-dimensional projection areas of particle images were used to calculate their equivalent circle area diameters, which are reported as particle sizes throughout this study.

Microparticle mass concentration values were calculated based on the fluid volume analyzed and the particle counts and sizes obtained from the VisualSpreadsheet software, using the particle spherical volume assumption and formulas summarized in the SI. Representative number-based and mass-based particle size distributions (PSDs) of microparticles detected in water samples from each bottle type, before and after sunlight exposure, are presented in SI4 (Fig. S5).

2.4. FTIR characterization of the plastic bottle material

Fourier transform infrared (FTIR) spectra of plastic material were acquired using the Thermo-Nicolet 6700 Series instrument. A flat section was cut from each bottle type, cleaned with ethanol to remove surface contaminants, and allowed to dry completely. Each cleaned sample was then placed on the attenuated total reflectance (ATR) crystal to ensure optimal contact and signal quality. Spectral acquisition was performed over the 4000–650 cm^{-1} range with a resolution of 4 cm^{-1}. A background scan was first performed to establish a baseline, followed by a sample scan averaging 32 scans to improve the signal-to-noise ratio. The resulting spectra were compared against reference spectra for plastic identification, and characteristic absorption peaks were interpreted to confirm the PET polymer type. The IR spectra collected before and after exposure are included in SI5 (Fig. S8).

2.5. TPD-DART-HRMS analysis

Water samples from twenty bottles exposed to sunlight for more than 30 days were combined and filtered using Whatman™ Grade 1 qualitative filter paper. The retained particulate residue was rinsed into 8 mL of HPLC-grade water and concentrated using a TurboVap® II evaporator (Biotage LLC). A 10 μL aliquot of the concentrated sample was transferred to a copper sample pot and placed onto the IonRocket™ heating stage (BioChromato Inc.), which was interfaced with a DART ionization source (JumpShot®, IonSense Inc.) and an Orbitrap Q Exactive HF-X high-resolution mass spectrometer (Thermo Scientific Inc.).[31,32] The heating stage, where evaporated species were ionized by metastable He* gas flow, was set to hold at 25 °C for 0.4 min, followed by a ramp at 70 °C min^{-1} to a final temperature of 600 °C, where it was kept for 2 min. High-resolution mass spectra were acquired in negative mode using Thermo Scientific Xcalibur software, and peak features were extracted with DeconTools Autoprocessor (**https://omics.pnl.gov/software/**). A custom Excel macro was employed to remove background signals by eliminating peak features associated with water blanks, known DART contaminants, ^{13}C isotopes, clusters, and m/z values with signal-to-noise ratios below 10. The same analytical procedure was applied to a sample of PET plastic material. Peak lists from the retained residue and the PET reference were then compared to identify HRMS features indicative of plastic-derived components in the water samples.

3. Results and discussion

3.1. Sunlight exposure profiles and cumulative photon dose quantification

Fig. 1 shows the cumulative photon dose received by PET water bottles over the 70-day exposure period. The inset plot displays the corresponding daily average photon fluxes throughout the experiment. Due to atmospheric attenuation, photon flux differs significantly between UVA (315–400 nm) and UVB (285–315 nm)
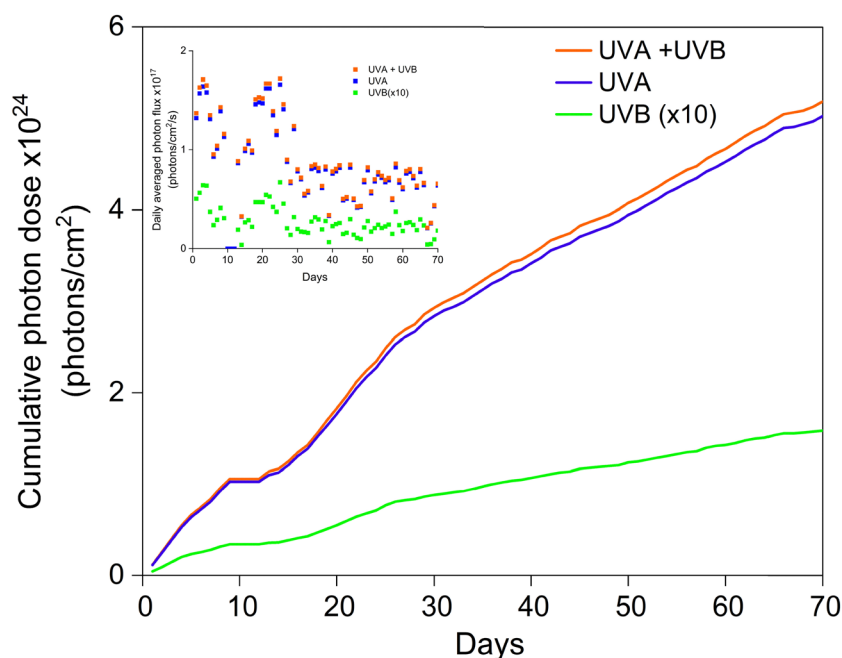

Fig. 1 Cumulative dose of the sunlight photons in UVA (315–400 nm) and UVB (285–315 nm) spectral ranges over the exposure period of 70 days. The daily average photon flux values are shown in an inset plot.

spectral regions, with UVB radiation being strongly absorbed by stratospheric ozone. In contrast, UVA – comprising approximately 95% of the UV radiation reaching Earth's surface – undergoes less atmospheric filtering.[33] In a context of the observations discussed below, photon dose values are used to quantify the extent of microparticle formation in bottled water, assuming that microparticles originate from plastic photodegradation, which is driven by the cumulative number of absorbed photons. The TUV model calculations shown in SI3 (Fig. S4b) were used to compare the solar irradiation conditions in our experiment with those typical of a representative SODIS region. Such regions experience consistently high solar radiation levels, minimal cloud cover and rainfall, and over 90% of sunlight reaching the surface as direct radiation.[20,21] The photon flux recorded in our study is approximately half that observed in the SODIS region, indicating that an equivalent photon dose could be accumulated in about half the time under typical SODIS conditions.

3.2. Microparticle release and mass accumulation from PET photodegradation

Fig. 2a presents representative particle images from water samples acquired using the FlowCam instrument. Microparticles were quantified by number-based and mass-based PSDs (Fig. 2b and SI4, Fig. S5, S6). The total particle number concentrations of $\sim 10^8$ mL^{-1} observed in this study are higher than previously reported values of $\sim 10^6$ mL^{-1} for bottled drinking water.[13,34] This discrepancy is likely due to differences in detection scope, as our measurements encompass a broader size range of colloidal particles, including, but not limited to, selectively identified microplastics, thereby resulting in higher overall particle counts. However, when considering only larger particles (>2 μm), our results are consistent with prior reports[13,34] as illustrated in SI4 (Fig. S7). Moreover, the observed mass loadings in our experiments are predominantly defined by large particles. Given that our detection threshold is approximately 300 nm, the contribution of smaller particles (<300 nm) to the total mass
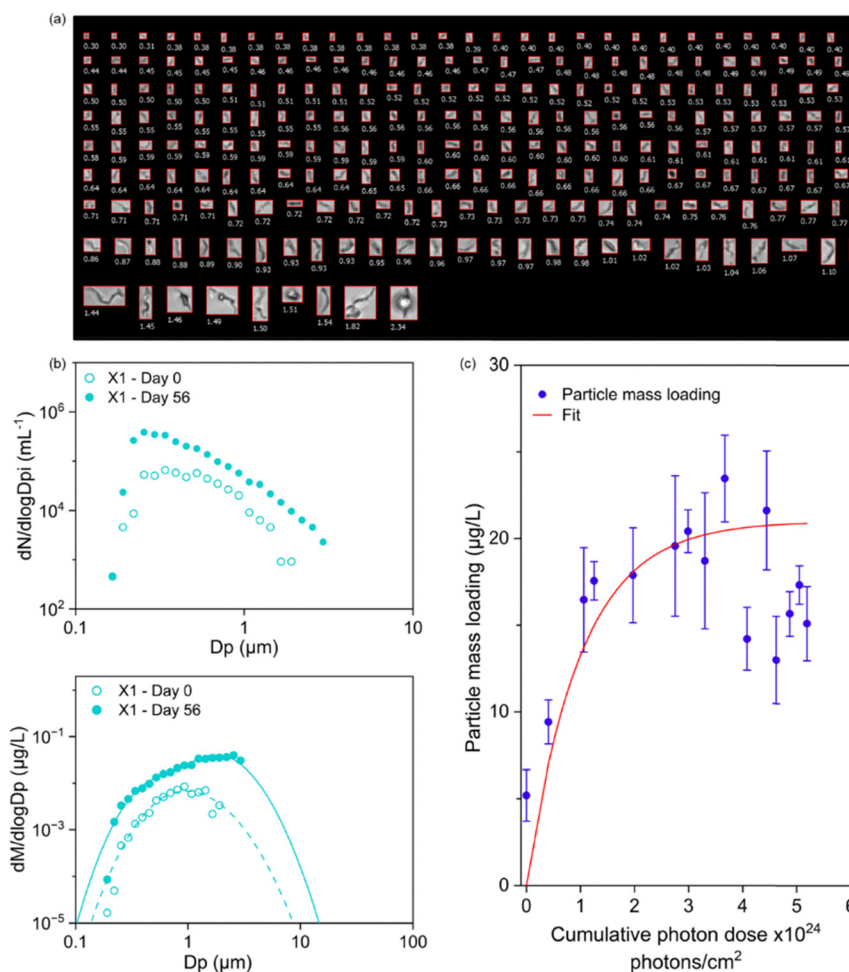
Fig. 2 (a) Illustrative FlowCam images of microparticles detected in bottled water; (b) representative number-based and mass-based PSDs of particles measured in water samples from X1 bottle type before and after 56 days of sunlight exposure. Individual symbols show experimental data, and lines show corresponding lognormal fit with dual modality, as outlined in SI4 (Tables S1–S5). (c) Mass loadings of microparticles averaged across all the plastic bottle types as a function of cumulative photon dose. The line represents the fit with a first-order photochemical reaction kinetics, quantifying mass loading changes as a function of photon dose.

loading was estimated by integrating lognormal PSD fits over the 0–300 nm range. For all datasets presented in Tables S1–S5, the calculated mass loadings of sub-300 nm particles are consistently well below 1 µg L^{-1}. Importantly, in colloidal system, small particles – even at high number concentrations – contribute very little to total mass. This underscores the importance of mass-based assessments: while smaller particles may be numerically dominant, their influence on total mass is minimal. For example, the combined mass of 1000 particles with a diameter of 300 nm is equivalent to that of a single 3 µm particle, underscoring the disproportionately large mass contribution of larger particles. Fig. 2c shows experimentally observed buildup of microparticle mass concentrations in the bottled water exposed to the sunlight irradiation, reaching values ranging between 14 ± 6 µg L^{-1} and 20 ± 6 µg L^{-1}. These mass concentrations are higher than those typically reported in tap water ($\sim$9 µg L^{-1}).[35,36] and drinking water treatment plants ($\sim$9.6 µg L^{-1}),[37] likely due to particle release associated with plastic photodegradation. As the PET bottle walls degrade under sunlight, more polymer fragments and particles are released, leading to higher mass concentrations relative to sources where such degradation is not a major factor.

Particle mass loading increases during the initial stages of sunlight exposure, consistent with previous findings.[38,39] However, the increase eventually reaches a plateau across all bottle types as shown in SI4 (Fig. S6), indicating the presence of limiting factors in the photodegradation process. One likely explanation is that photodegradation primarily occurs at the shallow water–plastic interface. As the interfacial plastic layers degrade, they may form degradation products that remain bound to the plastic surface, thereby reducing the interaction between the plastic and the surrounding water. This can slow the release of polymer fragments and particles into the water during prolonged sunlight exposure.[40] Furthermore, the composition and morphology of the PET surface in contact with water are heterogeneous, with regions of higher crystallinity likely offering greater resistance to photodegradation and particle release compared to more vulnerable amorphous regions.[41] The relative proportions of crystalline and amorphous domains can influence both the degradation kinetics and the mechanical detachment of fragments from the bottle surface. It is also possible that localized degradation within amorphous regions may proceed without leading to observable particle release, particularly when such regions are embedded within more crystalline domains.[41,42] Additionally, continued photodegradation of the released particles may contribute to the observed plateau. As these particles further fragment, they may fall below the detection threshold of our measurement technique. This suggests that while the observable mass accumulation stabilizes, ongoing degradation may still occur at the nanoscale, with smaller particles escaping detection.

The mass loadings buildup was modeled using first-order apparent photochemical kinetics, as described by eqn (1):

$$[\text{M}]_\phi = [\text{M}]_\infty \times (1 - \exp^{-k\phi}) \qquad (1)$$

where ϕ is the cumulative UVA + UVB photon dose incident on the water bottles (#photons cm^{-2}), $[\text{M}]_\infty$ is the asymptotic (terminal) mass loading of microparticles (µg L^{-1}), $[\text{M}]_\phi$ is the mass loading of microparticles after exposure to a photon dose ϕ, and k is the first-order photochemical rate constant (cm^2), representing the rate of particle mass buildup as a function of photon exposure. The values of $[\text{M}]_\infty$ and k were obtained by fitting eqn (1) to the experimental data. The fitted parameters are summarized in SI4 (Table S6), with the corresponding model fits and experimental data corresponding plots included in Fig. 2 and SI4 (Fig. S6). Baseline microparticle counts were non-zero at day 0, likely due to trace contaminants from bottling or handling. These were not subtracted in kinetic analyses (eqn (1)) to preserve the total microplastic burden under real-use conditions. The impact of these background levels on fitted kinetic parameters was minimal.
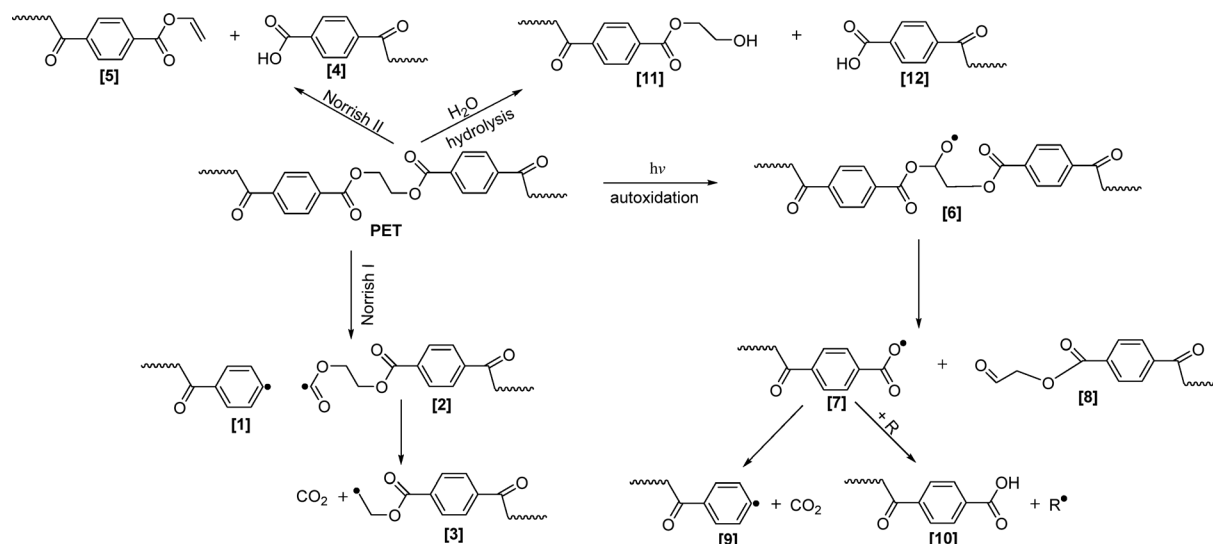
Scheme 1 PET photodegradation reactions.

The cumulative photon dose quantifies the total incident light exposure and reveals a clear relationship between sunlight intensity and the increase in particle mass within the water. Fig. 2c indicates that the particle mass loadings reach the plateau level after receiving a dose of $\sim 3 \times 10^{24}$ photons per cm^2, corresponding to approximately 30 days of exposure in our experiment and 15 days in the SODIS region. Overall, the particle mass loading values and the associated kinetic rates of their build-up appeared very consistent across different PET bottle types, suggesting that sunlight-induced degradation is the dominant factor driving microplastic release.

Scheme 1 summarizes the principal reaction pathways associated with the photochemical degradation of PET reported in the literature.[43] Upon UV irradiation, PET absorbs photons through its aromatic and carbonyl groups, promoting the formation of excited states that undergo Norrish type I and II reactions. The Norrish I reaction involves homolytic cleavage of bonds adjacent to carbonyl groups, yielding radical species (1) and (2), with subsequent fragmentation of (2) producing CO_2 and a smaller radical (3). In parallel, the Norrish II reaction induces ester bond cleavage, resulting in two closed-shell molecules with carboxylic acid (4) and vinyl (5) end groups. Further degradation is driven by autoxidation, initiated by UV-generated radicals and dissolved oxygen. This process leads to the formation of an intermediate containing hydroperoxide formed at the methylene group (6), followed by polymer chain scission that yields a carboxyl radical (7) and a stable fragment

bearing an aldehyde end group (8). The carboxyl radical can either undergo decarboxylation to generate CO_2 and a phenyl radical (9) or be stabilized via radical propagation, forming a carboxylic acid (10). These carboxylic acid products can themselves participate in photo-oxidative reactions, thereby further contributing to the PET degradation. In contact with water, it is also susceptible to hydrolytic degradation, yielding alcohol (11) and carboxylic acid (12) end groups. Consequently, the carboxylic acids generated through photodegradation may catalyze hydrolysis reactions at the PET–water interface. This implies that PET materials in contact with acidic water, such as in our X3 bottles, which contained lemon-flavored water with a pH of ~ 3, are more prone to hydrolytic degradation. However, no significant differences in microparticle release were observed compared to neutral pH samples, indicating pH was a minor factor under our experimental conditions.

3.3. FTIR analysis of PET degradation

We compared the FTIR spectra of unexposed PET plastics with those of the most sunlight-exposed samples (day 70) to assess chemical changes in PET resulting from photodegradation. Fig. 3a shows the IR spectrum of X1 plastic sample before and after sunlight exposure, representative of the spectral changes observed across all tested bottle types. The complete set of FTIR spectra, along with corresponding plastic wall thicknesses for the five bottle types, is provided in SI5 (Fig. S8), which also includes a tabulated list of PET characteristic vibrational bands annotated in
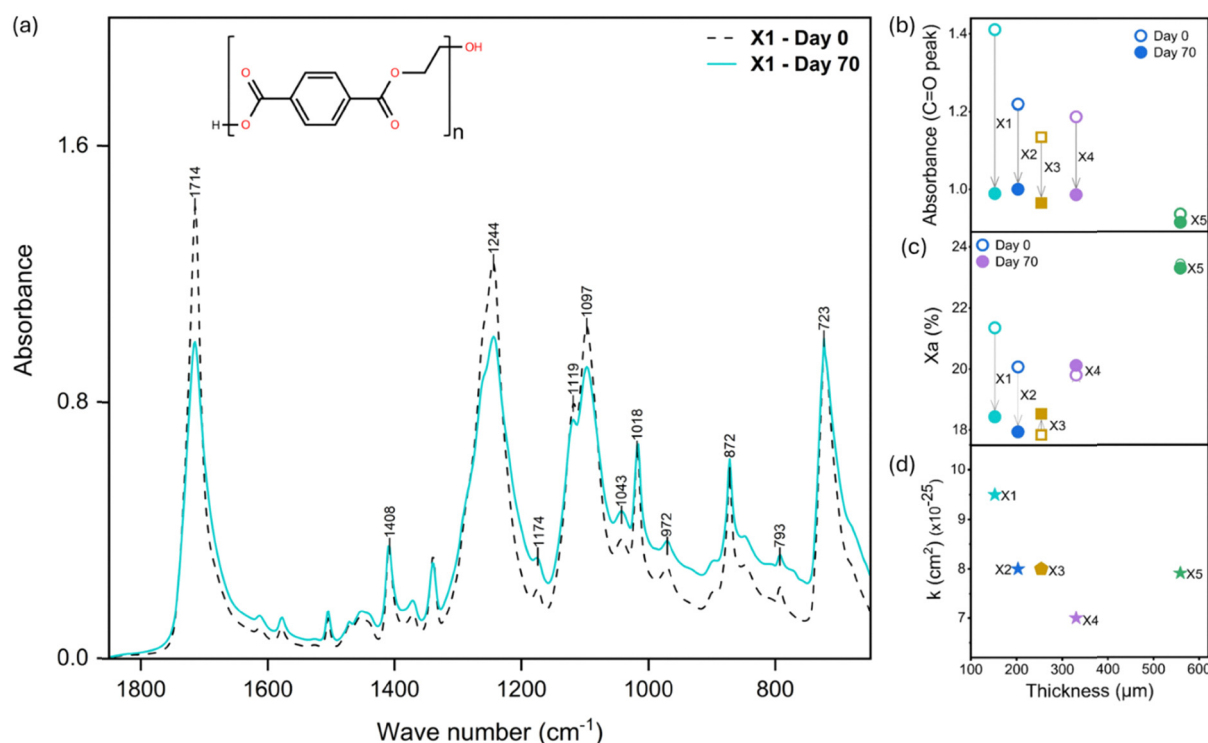
Fig. 3 (a) FTIR spectrum of PET material from X1 bottles before and after 70 days of sunlight exposure. Spectra from X2–X5 bottles are included in Fig. S9, along with annotated peak assignments. (b) Reduction in the $_\nu$[C=O] (1714 cm^{-1}) peak intensity as a function of bottle wall thickness. (c) Calculated amorphous fraction of each bottle type as a function of bottle wall thickness. (d) Kinetic degradation rate constant, k (cm^2), as a function of bottle wall thickness. The chemical structure of the PET monomer is included for reference.

the spectra.[44] The overall effects of PET photodegradation, as summarized in Scheme 1, can be assessed by examining changes in the ν[C=O] stretching band at 1714 cm^{-1}. Carbonyl groups within the PET backbone undergo photochemically induced reactions, resulting in decarboxylation (CO_2 loss)[45] and other chemical transformations leading to degradation and fragmentation of the PET polymer.[46,47] Accordingly, a decrease in the intensity of the ν[C=O] band following prolonged sunlight exposure serves as a spectroscopic marker for these degradation processes.[46] Fig. 3b compares the reduction of the ν[C=O] band observed for five bottle types with different wall thicknesses, revealing more pronounced changes in samples with thinner plastic walls. These observations suggest that increased plastic thickness may offer protective effects by reducing UV penetration and better preserving structural integrity, while thinner plastic bottles are more susceptible to photochemical degradation.[48] Another important factor influencing PET degradation is its semi-crystalline surface structure. Photochemical reactions occurring at the PET–water interface initiate microcrack formation that propagates into the polymer with continued UV exposure. This process promotes the leaching of low-molecular-weight fragments and the release of nano- and microplastic particles.[49,50] Most of the leached molecular products are poorly soluble in water and therefore either form colloidal aggregates or adsorb onto the surface of microplastic fragments. The resulting particles are polydisperse, exhibiting a wide range of sizes, morphologies, and compositions. Notably, the amorphous regions of the PET surface are more vulnerable to degradation, whereas crystalline domains exhibit greater resistance.[41]

The crystalline and amorphous fractions (X_c and X_a, %) of PET were estimated using the relative intensities of peaks at 1119 cm^{-1} (I_c) and 1097 cm^{-1} (I_a) within the broad ν[–C–O–] stretching band, following an established method[51] detailed in SI5 (and Table S7). Fig. 3c displays the calculated X_a values for each of the five bottle types, before and after 70 days of sunlight exposure, showing the X_a values in the range of 17–24%. While the trend in X_a appears to exhibit a U-shaped dependence on wall thickness, this variation likely reflects differences in PET produced by different manufacturers and should not be overgeneralized. Fig. 3d shows the corresponding values of the kinetic degradation rate constant (k) as a function of wall thickness, which similarly exhibits a U-shaped trend. The qualitative similarity between the X_a and k trends suggests that less oriented and more amorphous regions of PET are more vulnerable to photodegradation reactions and may cause faster degradation and release of microparticles into water.

3.4. Identification of PET degradation products *via* TPD-DART-HRMS

To confirm that the particles detected in the bottled water originate specifically from the plastic material, this study employs temperature-programmed desorption direct analysis in real-time high-resolution mass spectrometry (TPD-DART-HRMS).[32,52] This technique combines thermal desorption with ambient ionization, allowing direct analysis of condensed-phase samples without the need for extensive sample preparation. Its ability to detect a wide range of organic compounds makes it particularly well-suited for analyzing complex matrices such as polymers and environmental microplastics.[53–55] Fig. 4
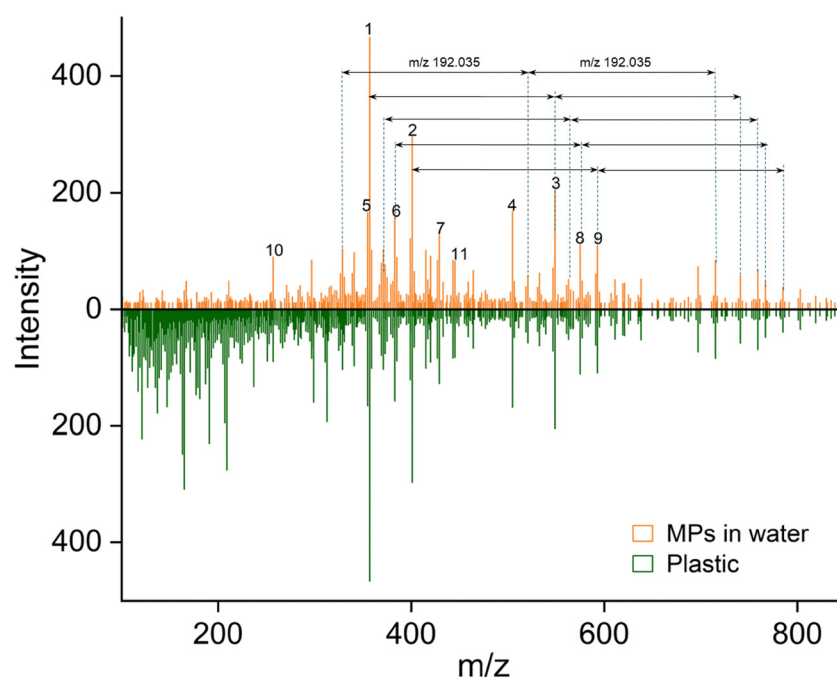
Fig. 4 (−)DART-HRMS plots comparing particulate residue filtered from exposed bottled water (orange) and dry plastic cut from the bottle (green). Spectra were averaged over the 2–7 min interval of the TPD thermograms (SI6, Fig. S9) to obtain representative mass profiles. Intensities are presented as the cubic root of the recorded signal to enhance visualization. Labeled peaks 1–11 indicate selected high-intensity features, with corresponding *m/z* values, elemental formulas, and tentative molecular structures provided in SI6 (Table S8).

compares the DART-HRMS spectra of filtered particulate residues collected from water in the sunlight-exposed bottles with that of the original PET plastic. Two spectra appear visually similar, and their molecular formula assignments reveal the presence of repeating units of terephthalic acid and ethylene glycol (m/z 192.035), consistent with the primary monomer of PET. In addition, modified terephthalate species were detected, which include hydroxylated dimers, transesterification products, and oxidized degradation products, summarized in SI6 (Table S8). It is important to emphasize that the detection of relatively low-molecular-weight fragments in Fig. 4 does not suggest that the microparticles themselves are composed exclusively of degradation products. Rather, the close correspondence in m/z values and relative signal intensities between the two spectra provides strong evidence of their common PET polymer identity. This conclusion is further supported by the consistency of these results with previous DART-MS analyses of PET reported in the literature.[56]

While Fig. 4 demonstrates that the major peaks in both spectra align, confirming a shared molecular composition, the spectrum of the filtered residue exhibits fewer low m/z peaks. This difference is attributed to the preconcentration step during sample preparation, which enhances the relative abundance of higher molecular weight fragments while volatilizing lower molecular weight species.[55,57,58] Despite these differences, the strong spectral overlap supports the conclusion that the detected residue originates from the plastic material itself rather than from external environmental contaminants. The findings indicate that prolonged UV exposure causes PET degradation through photooxidation and hydrolysis, leading to the release of structurally related microparticle residues into drinking water.[46,59,60]

4. Conclusion

This study identifies PET bottles as a source of microplastic contamination in drinking water. Although chemical fragments and microparticles associated with the PET degradation have low acute toxicity,[61] their small size increases the likelihood of translocation across biological barriers. Growing evidence has shown the presence of microplastics in human cells,[16,62] tissues,[8] brain,[63] and biological fluids.[64,65] Given that typical SODIS regions experience approximately twice the photon flux observed in our study, plastic degradation in such applications is expected to occur more rapidly, potentially leading to greater microplastic release. Our findings provide a quantitative framework for evaluating microparticle formation in bottled drinking water kept under solar exposure and suggest the need to explore alternative materials for solar water disinfection. Developing UV-resistant or biodegradable polymers may help reduce microparticle generation while maintaining disinfection effectiveness.

Author contributions

H. F. and A. L. designed the study. H.F., N. H., and K. B. conducted the experiments and analyzed data. H. F. and A. L. wrote the manuscript with contributions from all co-authors.

Conflicts of interest

There are no conflicts to declare.

Data availability

The data supporting this article are included in the SI.

Supplementary information is available. See DOI: https://doi.org/10.1039/d5sm00469a.

Acknowledgements

References

1 A. Ashrafy, A. A. Liza, M. N. Islam, M. M. Billah, S. T. Arafat, M. M. Rahman and S. M. Rahman, *J. Hazard. Mater. Adv.*, 2023, **9**, 100215.

2 M. Dheyaa, M. Hadeed and K. K. Al-Ahmady, *J. Pharm. Negat. Results*, 2022, 812–818.

3 D. Kankanige and S. Babel, *Sci. Total Environ.*, 2020, **717**, 137232.

4 B. E. Mann, G. Sarau, H. Holtmannspötter, M. Pischetsrieder, S. H. Christiansen and W. Dicke, *Water Res.*, 2018, **141**, 307–316.

5 A. Delre, M. Goudriaan, V. H. Morales, A. Vaksmaa, R. T. Ndhlovu, M. Baas, E. Keijzer, T. de Groot, E. Zeghal, M. Egger, T. Röckmann and H. Niemann, *Mar. Pollut. Bull.*, 2023, **187**, 114544.

6 A. Akinsemolu, *Sustainability*, 2023, **2**, 1–25.

7 Y. Li, L. Tao, Q. Wang, F. Wang, G. Li and M. Song, *Environ. Health*, 2023, **1**, 249–257.

8 P. Makhdoumi, A. A. Amin, H. Karimi, M. Pirsaheb, H. Kim and H. Hossini, *J. Water Process Eng.*, 2021, **39**, 101708.

9 E. Danopoulos, M. Twiddy and J. M. Rotchell, *PLoS One*, 2020, **15**, e0236838.

10 H. K. Webb, J. Arnott, R. J. Crawford and E. P. Ivanova, *Polymers*, 2013, **5**, 1–18.

11 A. Chamas, H. Moon, J. Zheng, Y. Qiu, T. Tabassum, J. H. Jang, M. Abu-Omar, S. L. Scott and S. Suh, *ACS Sustainable Chem. Eng.*, 2020, **8**, 3494–3511.

12 X. Wu, X. Chen, R. Jiang, J. You and G. Ouyang, *J. Hazard. Mater.*, 2022, **431**, 128523.

13 N. Qian, X. Gao, X. Lang, H. Deng, T. M. Bratu, Q. Chen, P. Stapleton, B. Yan and W. Min, *Proc. Natl. Acad. Sci. U. S. A.*, 2024, **121**, e2300582121.

14 S. Singh, T. Trushna, M. Kalyanasundaram, A. J. Tamhankar and V. Diwan, *Water Supply*, 2022, **22**, 5650–5674.

15 Y. Li, Z. Wang and B. Guan, *Environ. Res.*, 2022, **204**, 112134.

16 K. A. Hussain, S. Romanova, I. Okur, D. Zhang, J. Kuebler, X. Huang, B. Wang, L. Fernandez-Ballester, Y. Lu,

M. Schubert and Y. Li, *Environ. Sci. Technol.*, 2023, **57**, 9782–9792.

17 Y. Li, L. Peng, J. Fu, X. Dai and G. Wang, *Analyst*, 2022, **147**, 1099–1105.

18 L. Zimmermann, Z. Bartosova, K. Braun, J. Oehlmann, C. Völker and M. Wagner, *Environ. Sci. Technol.*, 2021, **55**, 11814–11823.

19 K. G. McGuigan, R. M. Conroy, H.-J. Mosler, M. D. Preez, E. Ubomba-Jaswa and P. Fernandez-Ibañez, *J. Hazard. Mater.*, 2012, **235–236**, 29–46.

20 K. O'Dowd, A. Martínez-García, I. Oller, M. I. Polo-López, S. Couso-Pérez, E. Ares-Mazás, H. Gómez-Couso, Á. García-Gil, J. Marugán, R. Marasini, K. G. McGuigan and S. C. Pillai, *J. Environ. Chem. Eng.*, 2023, **11**, 109787.

21 B. D. Bitew, Y. K. Gete, G. A. Biks and T. T. Adafrie, *Trials*, 2018, **19**, 412.

22 S. Murinda and S. Kraemer, *Phys. Chem. Earth*, 2008, **33**, 829–832.

23 B. Reyneke, T. C. Morris, P. Fernández-Ibáñez, K. G. McGuigan, A. Heida, K. A. Hamilton and W. Khan, *Water Biol. Secur.*, 2023, **20**, 100146.

24 C. Álvarez-Fernández, E. Matikainen, K. G. McGuigan, J. M. Andrade and J. Marugán, *J. Hazard. Mater.*, 2024, **465**, 133179.

25 P. Schmid, M. Kohler, R. Meierhofer, S. Luzi and M. Wegelin, *Water Res.*, 2008, **42**, 5054–5060.

26 J. S. Randhawa, *Bull. Natl. Res. Cent.*, 2023, **47**, 174.

27 Z. Huang, B. Hu and H. Wang, *Environ. Chem. Lett.*, 2023, **21**, 383–401.

28 S. Kim, Y. Hyeon and C. Park, *Molecules*, 2023, **28**, 6913.

29 Y. Hyeon, S. Kim, E. Ok and C. Park, *Chem. Eng. J.*, 2023, **454**, 140028.

30 N. Kaile, M. Lindivat, J. Elio, G. Thuestad, Q. G. Crowley and I. A. Hoell, *Front. Biosci.*, 2020, **7**, 552688.

31 E. Halpern, L. Heirty, C. West, Y. Li, W. M. Kim, A. S. Mennito and A. Laskin, *Environ. Sci.: Processes Impacts*, 2025, **27**, 104–118.

32 C. P. West, Y.-J. Hsu, K. T. MacFeely, S. M. Huston, B. P. Aridjis-Olivos, A. C. Morales and A. Laskin, *Anal. Chem.*, 2023, **95**, 7403–7408.

33 S. Singh, N. K. Lodhi, A. K. Mishra, S. Jose, S. N. Kumar and R. K. Kotnala, *Atmos. Environ.*, 2018, **188**, 60–70.

34 P. Zuccarello, M. Ferrante, A. Cristaldi, C. Copat, A. Grasso, D. Sangregorio, M. Fiore and G. Oliveri Conti, *Water Res.*, 2019, **157**, 365–371.

35 Y. Xu, Q. Ou, X. Wang, J. P. van der Hoek and G. Liu, *ACS EST Water*, 2024, **4**, 3348–3358.

36 Y. Li, Z. Wang and B. Guan, *Environ. Res.*, 2022, **204**, 112134.

37 A. Vega-Herrera, M. Llorca, X. Borrell-Diaz, P. E. Redondo-Hasselerharm, E. Abad, C. M. Villanueva and M. Farré, *Water Res.*, 2022, **220**, 118645.

38 W. Conradie, C. Dorfling, A. Chimphango, A. M. Booth, L. Sørensen and G. Akdogan, *Microplastics*, 2022, **1**, 456–476.

39 P. Xiang, T. Zhang, Q. Wu and Q. Li, *Sustainability*, 2023, **15**, 12698.

40 Y.-D. Lin, P.-H. Huang, Y.-W. Chen, C.-W. Hsieh, Y.-L. Tain, B.-H. Lee, C.-Y. Hou and M.-K. Shih, *Toxics*, 2023, **11**, 747.

41 N. F. Mendez, V. Sharma, M. Valsecchi, V. Pai, J. K. Lee, L. S. Schadler, A. J. Müller, S. Watson-Sanders, M. Dadmun, G. Kumaraswamy and S. K. Kumar, *Nat. Commun.*, 2025, **16**, 3051.

42 A. Samir, F. H. Ashour, A. A. A. Hakim and M. Bassyouni, *Npj Mater. Degrad.*, 2022, **6**, 68.

43 B. Gewert, M. M. Plassmann and M. MacLeod, *Environ. Sci.:Processes Impacts*, 2015, **17**, 1513–1521.

44 R. Chércoles Asensio, M. San Andrés Moya, J. M. De La Roja and M. Gómez, *Anal. Bioanal. Chem.*, 2009, **395**, 2081–2096.

45 Y.-W. Fu, W.-F. Sun and X. Wang, *Polymers*, 2020, **12**, 420.

46 E. Yousif and R. Haddad, *SpringerPlus*, 2013, **2**, 398.

47 Polymerization Reactions and Modifications of Polymers by Ionizing Radiation, https://www.mdpi.com/2073-4360/12/12/2877, accessed January 6, 2025.

48 A. G. Uzamurera, P.-Y. Wang, Z.-Y. Zhao, X.-P. Tao, R. Zhou, W.-Y. Wang, X.-B. Xiong, S. Wang, K. Wesly, H.-Y. Tao and Y.-C. Xiong, *J. Hazard. Mater.*, 2023, **448**, 130897.

49 A. L. Andrady, *Mar. Pollut. Bull.*, 2011, **62**, 1596–1605.

50 K. N. Fotopoulou and H. K. Karapanagioti, in *Hazardous Chemicals Associated with Plastics in the Marine Environment*, ed. H. Takada and H. K. Karapanagioti, Springer International Publishing, Cham, 2019, pp. 71–92.

51 Z. A. Kasuske, K. Arole, M. J. Green, T. A. Anderson and J. E. Cañas-Carrell, *Environ. Toxicol. Chem.*, 2025, **44**, 1525–1537.

52 E. Halpern, L. Heirty, C. West, Y. Li, W. M. Kim, A. S. Mennito and A. Laskin, *Environ. Sci.: Processes Impacts*, 2025, **27**, 104–118.

53 B. N. Peterson, A. C. Morales, J. M. Tomlin, C. G. W. Gorman, P. E. Christ, S. A. L. Sharpe, S. M. Huston, F. A. Rivera-Adorno, B. T. O'Callahan, M. Fraund, Y. Noh, P. Pahari, A. J. Whelton, P. Z. El-Khoury, R. C. Moffet, A. Zelenyuk and A. Laskin, *Environ. Sci.: Processes Impacts*, 2023, **25**, 1718–1731.

54 X. Zhang, A. Mell, F. Li, C. Thaysen, B. Musselman, J. Tice, D. Vukovic, C. Rochman, P. A. Helm and K. J. Jobst, *Anal. Chim. Acta*, 2020, **1100**, 107–117.

55 M. Fischer and B. M. Scholz-Böttcher, *Environ. Sci. Technol.*, 2017, **51**, 5052–5060.

56 Forensic Fiber Analysis by Thermal Desorption/Pyrolysis-Direct Analysis in Real Time-Mass Spectrometry|Analytical Chemistry, https://pubs.acs.org/doi/10.1021/acs.analchem.9b04167, accessed June 20, 2025.

57 Preconcentration – an overview|ScienceDirect Topics, https://www.sciencedirect.com/topics/chemistry/preconcentration, accessed February 6, 2025.

58 A. Navare, M. Nouzova, F. G. Noriega, S. Hernández-Martínez, C. Menzel and F. M. Fernández, *Rapid Commun. Mass Spectrom.*, 2009, **23**, 477–486.

59 T. Sang, C. J. Wallis, G. Hill and G. J. P. Britovsek, *Eur. Polym. J.*, 2020, **136**, 109873.

60 B. Gewert, M. Plassmann, O. Sandblom and M. MacLeod, *Environ. Sci. Technol. Lett.*, 2018, **5**, 272–276.

61 Registration Dossier – ECHA, https://echa.europa.eu/registration-dossier/-/registered-dossier/15563/7/1, accessed February 12, 2025.

62 H. Yadav, M. R. H. Khan, M. Quadir, K. A. Rusch, P. P. Mondal, M. Orr, E. G. Xu and S. M. Iskander, *Environ. Sci. Technol.*, 2023, **57**, 8225–8235.

63 A. J. Nihart, M. A. Garcia, E. El Hayek, R. Liu, M. Olewine, J. D. Kingston, E. F. Castillo, R. R. Gullapalli, T. Howard, B. Bleske, J. Scott, J. Gonzalez-Estrella, J. M. Gross, M. Spilde, N. L. Adolphi, D. F. Gallego, H. S. Jarrell, G. Dvorscak, M. E. Zuluaga-Ruiz, A. B. West and M. J. Campen, *Nat. Med.*, 2025, 1–6.

64 S. V. L. Leonard, C. R. Liddle, C. A. Atherall, E. Chapman, M. Watkins, S. D. J. Calaminus and J. M. Rotchell, *Environ. Int.*, 2024, **188**, 108751.

65 H. A. Leslie, M. J. M. van Velzen, S. H. Brandsma, A. D. Vethaak, J. J. Garcia-Vallejo and M. H. Lamoree, *Environ. Int.*, 2022, **163**, 107199.